

Repeated pulses of volcanism drove the end-Permian terrestrial crisis in northwest China

Received: 17 September 2023

Accepted: 12 August 2024

Published online: 02 September 2024

 Check for updates

Jacopo Dal Corso^{1,2}✉, Robert J. Newton¹✉, Aubrey L. Zerkle^{3,4}, Daoliang Chu², Haijun Song², Huyue Song², Li Tian², Jinnan Tong², Tommaso Di Rocco^{3,5}, Mark W. Claire^{3,4}, Tamsin A. Mather⁶, Tianchen He^{1,7}, Timothy Gallagher⁸, Wenchao Shu², Yuyang Wu², Simon H. Bottrell¹, Ian Metcalfe^{9,11}, Helen A. Cope¹, Martin Novak¹⁰, Robert A. Jamieson¹ & Paul B. Wignall¹

The Permo-Triassic mass extinction was linked to catastrophic environmental changes and large igneous province (LIP) volcanism. In addition to the widespread marine losses, the Permo-Triassic event was the most severe terrestrial ecological crisis in Earth's history and the only known mass extinction among insects, but the cause of extinction on land remains unclear. In this study, high-resolution Hg concentration records and multiple-archive S-isotope analyses of sediments from the Junggar Basin (China) provide evidence of repeated pulses of volcanic-S (acid rain) and increased Hg loading culminating in a crisis of terrestrial biota in the Junggar Basin coeval with the interval of LIP emplacement. Minor S-isotope analyses are, however, inconsistent with total ozone layer collapse. Our data suggest that LIP volcanism repeatedly stressed end-Permian terrestrial environments in the ~300 kyr preceding the marine extinction locally via S-driven acidification and deposition of Hg, and globally via pulsed addition of CO₂.

The Permo-Triassic mass extinction (PTME) was the most severe ecological disaster in Earth's history¹. The emplacement of the Siberian Traps large igneous province (LIP) with the release of large amounts of volcanic gases (including CO₂ and SO₂) into the atmosphere and in the ocean, and the consequent profound environmental changes are thought to have driven the collapse of all ecosystems from continental settings to the deep ocean². The marine extinction is well constrained to a relatively short interval of ~60 kyr across the Permo-Triassic boundary, but there is increasing evidence that the terrestrial crisis began tens to hundreds of thousands of years before the marine extinction³⁻⁷, for reasons as yet unknown.

Paleozoic-type forests disappeared suddenly in the latest Permian at most locations^{6,8,9}. The loss of terrestrial biomass was massive¹⁰ and probably unique in the geologic record. Furthermore, the PTME is the only known mass extinction of insects¹¹. The collapse of the base of the terrestrial food chain triggered the extinction at all higher levels^{12,13}. Lacustrine ecosystems collapsed and only recovered up to 10 Myr later in the Middle Triassic, beginning the so-called "Mesozoic lacustrine revolution"^{14,15}. The recovery of primary productivity on land took an exceptionally long time, as evidenced by a "coal gap" from the PTME to the early Middle Triassic, with thick coal measures not reappearing until the Late Triassic¹⁶.

¹School of Earth and Environment, University of Leeds, Leeds, UK. ²State Key Laboratory of Biogeology and Environmental Geology, School of Earth Sciences, China University of Geosciences Wuhan, Wuhan, China. ³School of Earth and Environmental Sciences and Centre for Exoplanet Science, University of St Andrews, St Andrews, UK. ⁴Blue Marble Space Institute of Science, Seattle, WA, USA. ⁵Geochemistry and Isotope Geology Department, Geosciences Center, University of Göttingen, Göttingen, Germany. ⁶Department of Earth Sciences, University of Oxford, Oxford, UK. ⁷College of Oceanography, Hohai University, Nanjing, China. ⁸Department of Geology, Kent State University, Kent, Ohio, USA. ⁹Division of Earth Science, School of Environmental and Rural Science, University of New England, Armidale, New South Wales, Australia. ¹⁰Department of Environmental Geochemistry and Biogeochemistry, Czech Geological Survey, Prague, Czech Republic. ¹¹Deceased: Ian Metcalfe. ✉e-mail: j.dalcorso@cug.edu.cn; r.j.newton@leeds.ac.uk

Several kill mechanisms have been proposed for the terrestrial crisis. A change from warm humid to unstable seasonal climate and a coeval increase in wildfire frequency, possibly caused by increasing $p\text{CO}_2$, global warming and storminess, are recorded in equatorial peatlands of South China at the level of the floral crisis⁴. Global cooling to intense warming in the Late Permian–Early Triassic, and unstable climates¹⁷ are thought to have driven a protracted extinction (up to -1 Myr) of tetrapods^{18,19}. Widespread mutagenesis amongst pollen and spores during the PTME has been attributed to atmospheric pollution and/or a rise in UV-B radiation caused by the depletion of the ozone layer by volcanic chemicals (SO_2 and halogens) from the Siberian Traps^{13,20,21}. Evidence of an increased UV-B flux—and therefore a depleted ozone layer—across the broad interval containing both marine and terrestrial extinctions, comes from the observation of increased concentrations of UV-B absorbing compounds in sporomorphs²², but these records are of low resolution and correlation with the precise level of the terrestrial extinction is not proven. S-isotope data from continental fluvial PTME successions of the Karoo Basin (South Africa) and the Sydney Basin (Australia) may indicate increased S deposition in these environments^{23,24}. In particular, the Late Permian–Early Triassic pyrite-sulfur isotope records of Li et al.²³ show a broad, long-term negative shift starting at the extinction level and spanning the entire Griesbachian and part of the Dienerian that has been interpreted as evidence of an increase in sulfate concentrations in the atmosphere. Metal poisoning has also been proposed to explain the extinction on land, but in terrestrial successions of South China, increases of Hg and Cu concentrations are found in strata above the crisis, along with unseparated spore tetrads of surviving plants²⁵.

To explore the linked hypotheses related to the impact of volcanism on terrestrial ecosystems, we performed high-resolution S, Hg, and C geochemistry of the latest Permian–earliest Triassic middle latitude continental successions of the Junggar Basin in northwest China (Xinjiang; Fig. 1 and Supplementary Fig. S1, and “Methods”). The bedrock geology of the catchment in the late Permian consisted of mainly coarse-grained continental sediments interbedded with volcanic facies²⁶, which are likely to have low sulfur contents, enhancing the site’s potential to record changes in atmospheric inputs by limiting concentrations of weathered sulfate. To track the addition of volcanic sulfur to the terrestrial system, we analyzed carbonate-associated sulfate (CAS) from palaeosol and lacustrine carbonates in wholly terrestrial and lake margin settings (Taodonggou and Tarlong sections; Supplementary Fig. S1); Sulfate is not retained in most terrestrial sediments because it is too soluble, but palaeosol nodules and freshwater limestones can preserve syngenetic CAS and its pristine isotopic composition. We analyzed total sulfur $\delta^{34}\text{S}$, organic $\delta^{13}\text{C}$ and Hg concentrations from nearby lake sediments (Dalongkou North section) with a well-constrained record of extinction in lacustrine fauna and surrounding flora (Fig. 2; e.g., ref. 27) to provide a robust connection between volcanism, increased sulfate deposition, potential metal poisoning, and terrestrial extinction. We also analyzed the minor sulfur isotope composition of selected samples to test for the effects of ozone layer destruction.

Results

In the Dalongkou North lacustrine section, total organic matter (TOC) is generally low ($<1\text{ wt}\%$; Fig. 2). On average, TOC is higher before the extinction ($\sim 0.5\text{ wt}\%$, with peaks $>2\text{ wt}\%$) than after ($\sim 0.2\text{ wt}\%$) (Fig. 2 and “Methods” for the definition of the extinction level in the Junggar Basin). The C-isotope composition of TOC ($\delta^{13}\text{C}_{\text{org}}$) displays an -8% negative C-isotope excursion (NCIE) in beds 16–18 of the studied section, and a -5% NCIE in beds 22–24 at the level of the extinction of conchostracans, ostracods and *Charophyte* taxa²⁷, and a third, partial NCIE, in the uppermost part of the studied section, beds 37–42 (Fig. 2). The profile of our $\delta^{13}\text{C}_{\text{org}}$ data is similar to a previous lower-resolution $\delta^{13}\text{C}_{\text{org}}$ record from the same section²¹ (Fig. 2), from the south limb of

the Dalongkou anticline, and from Taodonggou section^{28,29} (Fig. 2). The $\delta^{13}\text{C}_{\text{org}}$ curve of Dalongkou North can be correlated with marine²⁸ and other terrestrial records³⁰, where a similar decline of TOC is also observed⁴.

$\delta^{34}\text{S}_{\text{CAS}}$ data from palaeosol and lacustrine carbonates of the Tarlong and Taodonggou sections have a range of -9 – 12% at the base of the sections with a shift toward less positive values in the range 5 – 6.5% . The $\delta^{34}\text{S}_{\text{CAS}}$ shift in palaeosol carbonates starts at the second NCIE in the Taodonggou section, which corresponds to the extinction level at Dalongkou (Fig. 3). We note a possible diachrony between the freshwater and palaeosol carbonate $\delta^{34}\text{S}_{\text{CAS}}$ shifts at Tarlong, but this is a result of a single negative palaeosol datapoint at 129 m so may not be real. This is followed by a rebound toward pre-excursion values. The $\delta^{34}\text{S}_{\text{CAS}}$ negative shift is coupled to an increase in CAS concentration in the lacustrine limestone samples close to the point at which their $\delta^{34}\text{S}_{\text{CAS}}$ declines (Fig. 3), while the CAS concentration in the palaeosol carbonates is much more varied (Supplementary Fig. S2). Because S-deposition can be linked to acidification, carbonates may be prevented from forming during intense depositional events. We would therefore expect that these carbonates record the average background loading of atmospheric sulfate in soils (palaeosol) and lake waters (freshwater limestones) of the catchment.

Yields of Ag_2S recovered after chromium extraction in selected samples show low pyrite contents (Supplementary excel file), hence the decision to extract total-S for S-isotope ($\delta^{34}\text{S}_{\text{TOT}}$) analyses. Total-S is assumed to represent reduced forms of sulfur in the sediment, i.e., sulfides and organic-S (Fig. 1). $\delta^{34}\text{S}_{\text{TOT}}$ from Dalongkou North fluctuate between $+6$ and -7% and record repeated large -9 – 10% negative shifts in the lower part of the section, i.e., before the second NCIE (meters -10 to 85), where major peaks of Hg concentrations ($>100\text{ ppm}$) and Hg/TOC (up to ca. 300 – $600\text{ ppm/wt}\%$) are also recorded (Fig. 4). The negative $\delta^{34}\text{S}_{\text{TOT}}$ shifts are coupled to the increases in Hg and Hg/TOC (Fig. 2; Supplementary Fig. S3). Total-S concentrations at Dalongkou are generally low but variable, with higher peaks in the interval below the oldest NCIE, transitioning to more consistently low concentrations in the upper part of the section (Fig. 4).

At Dalongkou North, minor S-isotope analysis of samples with larger yields of extracted S (see “Methods”) shows $\Delta^{33}\text{S}$ values between -0.093% and 0.147% , and $\Delta^{36}\text{S}$ from -0.956% and 1.192% in total sulfur (Fig. 5). CAS $\Delta^{33}\text{S}$ and $\Delta^{36}\text{S}$ data from the palaeosols at Tarlong lie in a narrower range (-0.01% to 0.062%) and show no major changes along the section (Fig. 5). $\Delta^{33}\text{S}$ vs $\Delta^{36}\text{S}$ data are linearly correlated with a slope = -6.43 ± 1.03 (Supplementary Fig. S4), which is a pattern typical of S-isotope mass-dependent fractionation, (S-MDF; $\Delta^{36}\text{S} = -6.85\Delta^{33}\text{S}$; e.g., ref. 31). Within this range of S-MDF, $\Delta^{33}\text{S}$ and $\Delta^{36}\text{S}$ values fluctuate through the section, with the negative $\Delta^{33}\text{S}$ shifts mostly coupled to positive shifts of $\Delta^{36}\text{S}$, negative $\delta^{34}\text{S}_{\text{TOT}}$ values and peaks of Hg and Hg/TOC (Fig. 5).

Discussion

An increase in reduced sulfur input to the catchment coincident with terrestrial extinction

Carbonate-associated sulfate captures the isotopic signal of the fluid from which the carbonate precipitated with negligible fractionation³² but has almost exclusively been applied to carbonates formed in the ocean. Soil-formed carbonate extracted with similar techniques has been previously shown to record the minor oxygen isotope composition of atmospheric sulfate at a number of modern sites³³. Our records of $\delta^{34}\text{S}_{\text{CAS}}$ in palaeosol and lacustrine carbonate agree well with each other, suggesting that they are a good representation of sulfate within the catchment (see “Discussion” in the Supplementary Information).

The oldest sediments have a baseline signature of approximately 12% . Sulfate from seawater is an important component of modern atmospheric sulfate deposition³⁴. The similarity of background $\delta^{34}\text{S}_{\text{CAS}}$

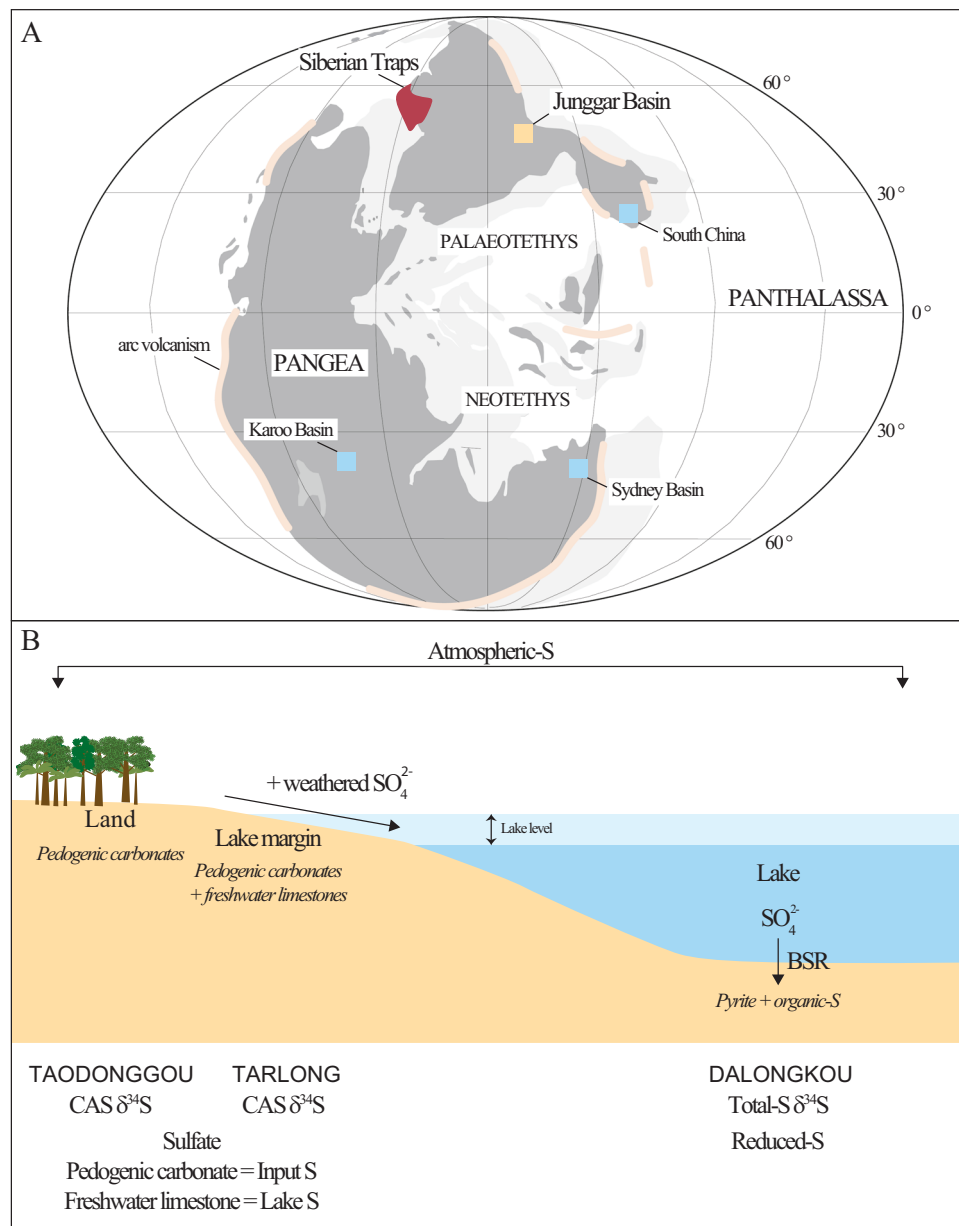


Fig. 1 | Palaeolocation and depositional environment of the studied sections. **A** A map of the global end-Permian paleogeography (Light gray = shelf areas; dark gray = land) with the location of the studied sedimentary successions in a fluvio-lacustrine environment in the Junggar Basin, now in the Bogda Mountains of Xinjiang, northwest China (Supplementary Fig. S1) indicated, as well as the locations of other important records referred to in the text (light blue squares), the Siberian traps (dark red) and arc volcanism (light red lines). **B** A schematic showing the depositional environment of the studied sections: The three sections were chosen because they represent three different depositional environments within the land-lake ecosystem. The Taodonggou series was deposited in a fluvial-mudflat

environment²⁹ containing palaeosols with pedogenic carbonate nodules. The Tarlong section is located in the lake margin and contains both pedogenic carbonates and freshwater limestones²⁹. The Guodikeng Fm. at Dalongkou North was deposited in the lake³². The three sections therefore contain different sulfur archives (pedogenic and freshwater carbonates, pyrite and organic-S), in which S-isotope signatures reflect S inputs and fractionation processes occurring in the lacustrine environment during the end of the Permian. CAS carbonate-associated sulfate, BSR bacterial sulfate reduction. Paleogeography after ref. 103. Position of arc magmatism after ref. 63.

to coeval evaporite $\delta^{34}\text{S}$ values³⁵ suggests that this was also the case in the Junggar Basin prior to the extinction, with the sea spray blown to the depositional site from the Panthalassa Ocean margin >1000 km to the east, and is consistent with a negligible contribution of weathered sulfate from the catchment, which consisted of mainly coarse-grained sediments and volcanic rocks²⁶, likely to have low sulfur contents (Supplementary Information).

There are a range of processes that could account for the observed decline in $\delta^{34}\text{S}_{\text{CAS}}$, which reaches its most negative values around the time of the second NCIE and terrestrial extinction (Fig. 3).

Sulfur deposition from the atmosphere is sourced from a mixture of seawater sulfate and reduced sulfur compounds produced by biogenic processes either in the ocean or on land (e.g., hydrogen sulfide, dimethyl sulfide, carbonyl sulfide), which, although variable, commonly have a more negative $\delta^{34}\text{S}$ when compared to seawater³⁶. Volcanically derived atmospheric sulfur or pyrite in the bedrock would also be expected to have a more negative isotope signal³⁷. The decline in $\delta^{34}\text{S}_{\text{CAS}}$ in the records from the Junggar Basin can be most plausibly explained by an increase in the proportion of reduced sulfur being delivered to the catchment (see “Discussion” in Supplementary

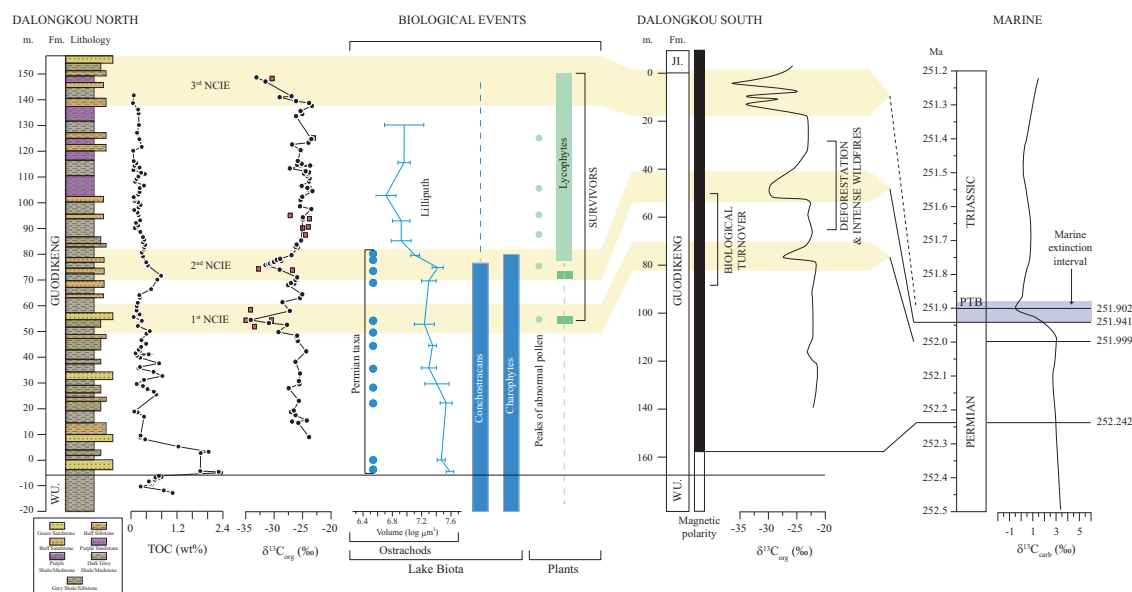


Fig. 2 | Organic C-isotope changes and major biological events recorded at Dalongkou (Junggar Basin, Bogda Mountains, China), and correlation with the marine mass extinction. Three negative C-isotope excursions (NCIEs) are recorded in the organic matter ($\delta^{13}\text{C}_{\text{org}}$) at Dalongkou: dots are new data from this study, and red squares are data from ref. 21. The 2nd NCIE is coincident with the ecosystem crisis, as recorded by the appearance of mutated pollen²¹ and an increase in the abundance of surviving lycophytes, the extinction of conchostracan and charophyte taxa, followed by a post-extinction small (Lilliput) ostracod fauna²⁷. Total organic carbon (TOC) concentrations also decreased during the terrestrial

crisis. In this study, the Dalongkou North section has been analyzed. The nearby Dalongkou South section has been previously correlated to the marine record^{28,60}, providing a timeframe for the changes observed in the terrestrial Junggar Basin. At Dalongkou South, deforestation and intense wildfires are recorded at an interval across the 2nd NCIE¹⁰⁴. U/Pb ID-TIMS analysis of bentonites from the Tarlong-Taodonggou area provides ages of 253.11 ± 0.05 Ma and 253.63 ± 0.24 Ma for the lower part of the Guodikeng Formation⁶¹. The last coal bed in the succession of the Bogda Mountains occurs at an estimated age of 252.29 Ma⁵⁹. W.U. = Wutonggou formation. J.I. = Jiucuiyuan formation. Source data are provided as a Source Data file.

Information). For example, it is possible to change the ratio of reduced sulfur to sea spray sulfur if the distance to the coast were to increase via sea level fall because sea spray forms large particles, and their deposition declines with distance from the ocean shoreline³⁸. However, the decline in $\delta^{34}\text{S}_{\text{CAS}}$ correlates with a transgression, rather than a regression, representing the whole Guodikeng Formation^{28,29}, so this explanation is unlikely. The apparent diachrony between the freshwater and palaeosol carbonate $\delta^{34}\text{S}_{\text{CAS}}$ shifts is here interpreted as an artifact of the record. As also explained below, those carbonate archives record snapshots of the $\delta^{34}\text{S}_{\text{CAS}}$ in the system that could hide a more complex dynamic of multiple excursions alternating with no precipitation of carbonates in the soil and lake margin.

The controls on CAS concentration are not well understood, but sulfate concentration, the ratio of dissolved sulfate to carbonate and mineral growth rate have been shown to be important in various settings^{39–41}. The amount of CAS in soil carbonates is likely to be highly heterogeneous and will reflect the localized balance of calcium, carbonate and sulfate ions in these waters at the time of mineral precipitation. Lake waters are likely to be much more homogenous with respect to sulfate and other chemical variables at any given time point and therefore might be expected to represent a more consistent record of regional environmental conditions. The increase of CAS concentration in the lacustrine limestones (Fig. 3) occurs concurrently with the decrease in $\delta^{34}\text{S}_{\text{CAS}}$ and is consistent with increases in sulfate concentration in lake waters and/or an increase in the sulfate to carbonate ion ratio driven by declining pH.

Multiple pulses of atmospheric S deposition recorded in the lacustrine environment

Changes in S inputs to lakes are recorded in the concentration and isotopic composition of S in their sediments⁴². However, if there are other concurrent changes in environmental conditions within the lake, the sediment S geochemical and isotopic signals may be affected by

more than one process. The S stored in lake sediments does not necessarily have the same isotopic composition as the lake water and can be stored in three forms: lake-water sulfate trapped in precipitated minerals, e.g., carbonate, with little or no S isotope fractionation, organic-S derived from plant material, which has similar $\delta^{34}\text{S}$ to the lake water^{43,44}, and diagenetic sulfide incorporated later into the sediment either as organic-S or as sulfide minerals, commonly FeS or pyrite^{45–47}. Sulfate-reducing microbes discriminate strongly in favor of the lighter (³²S) isotope when reducing sulfate, and thus, the sulfide formed has lower $\delta^{34}\text{S}$ than the lake-water sulfate^{48,49}. However, when sulfate concentrations are low, a large proportion of the total sulfate is converted to sulfide, which then has a S isotope composition similar to the original sulfate⁵⁰. Thus, if sulfate concentrations are low, and sulfate sources (and S isotope compositions) change but sulfate concentration does not, the isotopic composition of sulfur in the sediment will closely track the changing isotopic composition of the sulfate sources. If changes to sulfate sources are accompanied by increasing sulfate concentrations, then changes in the net S isotope fractionation between lake-water sulfate and the diagenetic sulfide incorporated into the sediment may occur, as sulfate is no longer limiting. In this case, the sediment sulfur $\delta^{34}\text{S}$ will reflect not only isotopic changes in the sulfate source but also in lake sulfate concentration via an increase in the expression of negative S isotope fractionation in the diagenetic component at higher sulfate concentrations^{49,51}.

The $\delta^{34}\text{S}_{\text{TOT}}$ from Dalongkou North displays a series of large negative shifts of approximately 9–10‰ prior to, and coincident with, the second NCIE (–10 to 85 m in section; Fig. 4). These data suggest repeated discrete inputs of S to the lake, from a different, more ³⁴S-depleted source, and/or increased lake sulfate concentrations and greater fractionation effects during sulfate reduction under less sulfate-limiting conditions. Although occurring roughly in the same stratigraphic interval within the Guodikeng Fm., the multiple negative $\delta^{34}\text{S}_{\text{TOT}}$ shifts are not observed in the $\delta^{34}\text{S}_{\text{CAS}}$ record, which shows just a

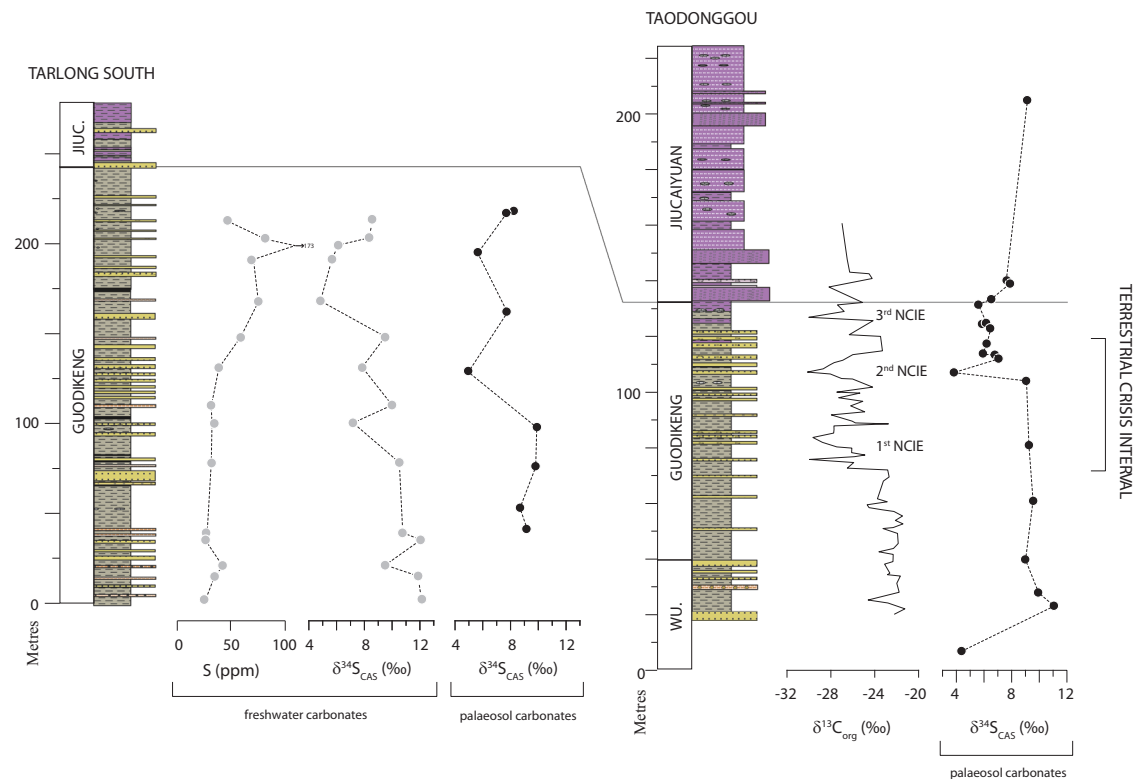


Fig. 3 | Higher atmospheric S deposition during the end-Permian crisis on land.

An increase in CAS concentration in the freshwater limestones, and synchronous decrease in carbonate associate sulfate S-isotope ($\delta^{34}\text{S}_{\text{CAS}}$) values in freshwater limestones and pedogenic carbonates in the lake margin Tarlong section, and in the pedogenic carbonates in the fully terrestrial Taodonggou section. S concentrations in palaeosols from Taodonggou and Tarlong are available in the supplementary data. They are not presented in this figure because there is less reason to suppose that

they hold meaningful environmental information (see main text), and when plotted, they show no relationship with the isotope events. The Permian–Triassic boundary is close to the boundary between the Guodikeng and Jiuciyuan formations (see also Fig. 2). C-isotope data at Taodonggou section is from refs. 28,29. NCIE negative C-isotope excursion, WU, Wutonggou formation, JIUC, Jiuciyuan formation. Source data are provided as a Source Data file.

broader negative excursion starting from the second NCIE (Fig. 3). The lake succession of Dalongkou North is a more continuous record of reduced sulfur deposition than the land–lake margin palaeosol and freshwater carbonates of Taodonggou and Tarlong, which record more sporadic snapshots of the isotopic composition of sulfate in the system, as mentioned above. In addition, because the volcanic pulses are likely to have been accompanied by H^+ ions from various sources (including but not limited to H_2SO_4), times of peak deposition may have actively prevented carbonate precipitation in the basin. The palaeosol and freshwater CAS records should therefore be viewed as the long-term background perturbation to the sulfate retained in the catchment.

The CAS concentration data from the lacustrine limestones and S-isotope data from the limestones and soil carbonates support both increases in lake sulfate concentration and a change to a more ^{34}S -depleted source isotope composition. Lake sulfate concentrations can also be increased by decreases in lake volume and/or increased weathering. Evidence of weathering changes is recorded in the Junggar Basin by a lithological change to coarser-grained material, which defines the transition from the Guodikeng Formation to the overlying Jiuciyuan Formation⁵². This lithological change is much higher in the Dalongkou North section and therefore significantly younger than the negative $\delta^{34}\text{S}_{\text{TOT}}$ excursions we report here. Both changing lake level and increased weathering would be expected to be accompanied by coeval changes in sedimentology, but this does not systematically covary with $\delta^{34}\text{S}_{\text{TOT}}$, suggesting that neither was an important influence on our record (Fig. 4). The absence of grain size changes during the cycles of $\delta^{34}\text{S}_{\text{TOT}}$ also suggest that changes in sedimentation rate did not exert a significant control, as has been evidenced for some

marine systems⁵³. Major redox variations in the lake are not recorded in the sedimentary and paleontological record of Dalongkou North (e.g., the presence of Conchostracans), and are therefore excluded as significantly affecting our record.

The preservation of sulfur as pyrite and organic-S, and therefore the ability of the sediments to record changes in lake S cycling, is dependent on the flux of organic carbon to lake sediments. Due to the dependence of S preservation on TOC, it might be expected that S/TOC would record S pulses into the basin⁵⁴, but only if TOC was constant. However, TOC is highly variable (0.1 to 2.4 wt%, mean 0.5 wt%, between -12.8 and 90 m) up to approximately the time of extinction (Fig. 4) and is likely controlled by a range of factors such as nutrient availability, sedimentation rate and the balance of land plant and lake derived organic matter. These factors do not necessarily respond to S inputs, and this likely accounts for the lack of relationship between S/TOC and $\delta^{34}\text{S}_{\text{TOT}}$. TOC becomes uniformly low above 90 m at Dalongkou North (0.03 to 0.36 wt%, mean 0.17 wt%, between 90 and 142 m) shortly after the start of the terrestrial extinction interval (Fig. 4), indicating that the lack of further $\delta^{34}\text{S}_{\text{TOT}}$ excursions could either be due to the cessation of S pulses to the basin or simply the loss of the potential to record them. In this respect, the presence of less positive values in the land–lake margin records of Tarlong and Taodonggou after the second NCIE (Fig. 3) indicate that the second option is the most likely.

Using average $\delta^{34}\text{S}_{\text{CAS}}$ values for the pre-NCIE-2 (+9.7‰) and NCIE-2 to -3 (+6.6‰) intervals from Taodonggou and Tarlong we can estimate enrichment factors ($\epsilon^{34}\text{S}$) between sulfate and total-S in the lake sediments in the same intervals. These vary between 0 and 5‰ during the most positive parts of the $\delta^{34}\text{S}_{\text{TOT}}$ curve to 11–16‰ when $\delta^{34}\text{S}_{\text{TOT}}$ is

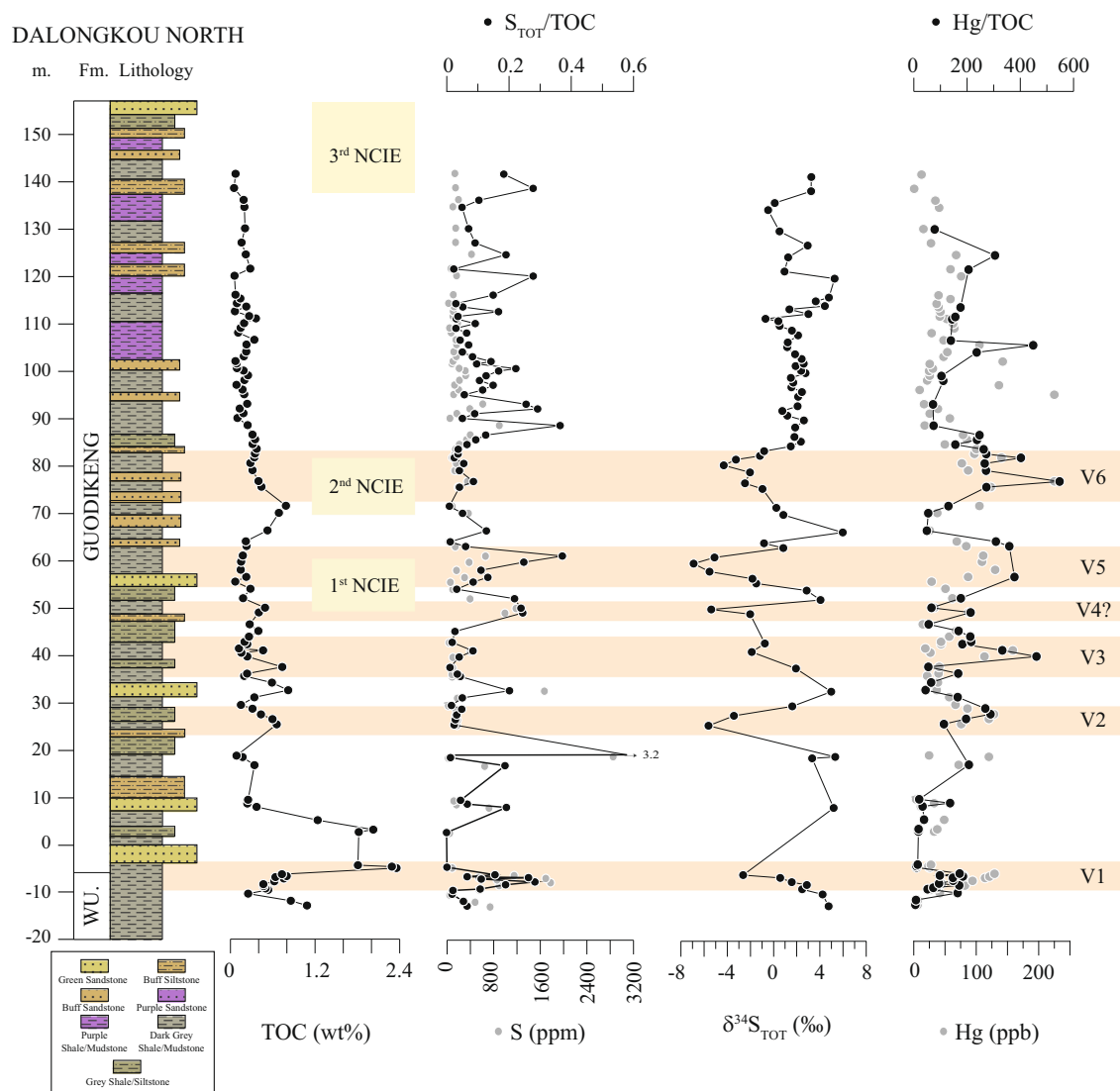


Fig. 4 | Inputs of volcanic S and Hg to the end-Permian lacustrine environment. The geochemical record shows spikes in Hg/TOC and negative shifts in total S-isotope ($\delta^{34}\text{S}_{\text{TOT}}$) at Dalongkou North. V1–V6 highlight paired Hg/TOC and

$\delta^{34}\text{S}_{\text{TOT}}$ spikes. NCIE negative C-isotope excursion, TOC total organic carbon, WU. Wutonggou formation. Source data are provided as a Source Data file.

at its most negative. The latter may not represent a good estimate because carbonates may be systematically excluded from deposition during these events because of acid deposition. Enrichments between sulfate and sulfide have been previously used to estimate sulfate concentrations, and the very small $\epsilon^{34}\text{S}$ during background deposition suggests lake sulfate concentrations $<100\ \mu\text{M}^{55}$. The reduction in TOC that occurs after NCIE-2 means that $\epsilon^{34}\text{S}$ is unlikely to record the changes in lake concentration, which are suggested by the increase in limestone CAS concentration, after this point. Overall, our combined CAS and $\delta^{34}\text{S}_{\text{TOT}}$ data support multiple discrete additions of ^{34}S -depleted S to the lacustrine environment, and the lack of a sedimentological response in concert with these perturbations suggests that this came from the atmosphere.

Volcanic pulses of Hg and S to the lake catchment

The multiple Hg and Hg/TOC spikes that are coupled to the negative $\delta^{34}\text{S}_{\text{TOT}}$ shifts in the lower part of the section up to the second NCIE (V1–V6 in Fig. 4) indicate that the increases in atmospheric S deposition in the lacustrine ecosystems were likely to be derived from volcanic activity. Peaks in Hg concentration and Hg/TOC recorded after the second NCIE may also represent increases in volcanic-sourced Hg

to the basin, but they lack the support of concurrent S-isotope shifts. As mentioned before, this may be explained by a loss of capacity of the system to bury sulfur, as TOC values are consistently very low in this part of the section (Fig. 4).

Records from coastal and marine environments show one or two discrete spikes in Hg and Hg/TOC at the marine extinction level, coupled with a negative shift in Hg isotopes^{56,57}. These spikes occur within an interval with generally higher background Hg concentrations during the PTME^{2,58}. Modeling suggests that while the longer-term Hg concentration increase can be attributed to volcanism, the large spike within this interval, which is recorded both in terrestrial and marine successions, is best explained by massive and rapid (~1000 years) oxidation of soil organic matter linked to the collapse of ecosystems on land¹⁰. Within the smaller reservoir of the lake experiencing high sedimentation rates, relatively brief pulses of volcanic Hg could have been more easily recorded. The Dalongkou North section is expanded, and therefore the temporal resolution of the geochemical data is higher, allowing a better resolution of discrete changes in Hg loading. Higher Hg drawdown due to euxinic conditions can be excluded due to the lack of sedimentological and paleontological evidence for major redox changes in the lake (see “Geological setting”). As explained

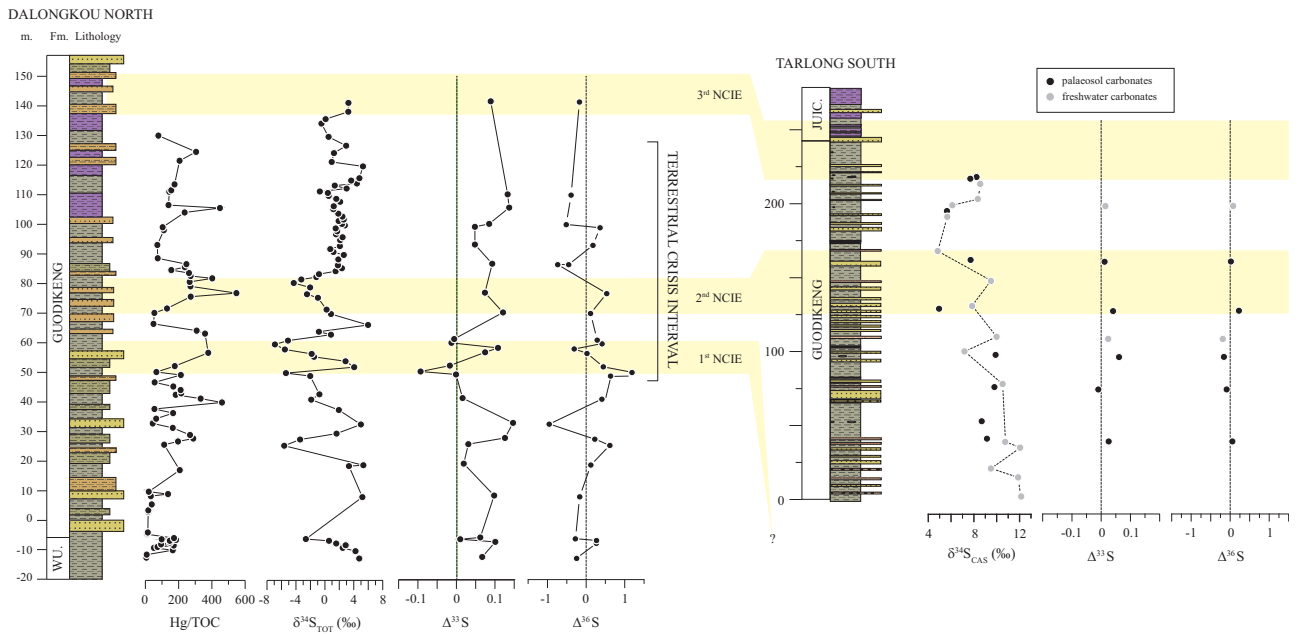


Fig. 5 | Near-zero minor S-isotope signatures in terrestrial archives during the end-Permian. $\Delta^{33}\text{S}$ and $\Delta^{36}\text{S}$ data from Dalongkou North and Tarlong South fall within the values indicating biological mass-dependent processes (see Supplementary Fig. S4), inconsistent with significant UV-B radiation and photoreduction

of SO_2 . The correlation between the lacustrine Dalongkou North section and the lake margin Tarlong section is based on previous stratigraphic considerations^{28,29}. WU, Wutonggou formation, JIUC, Jiuciyuan formation. Source data are provided as a Source Data file.

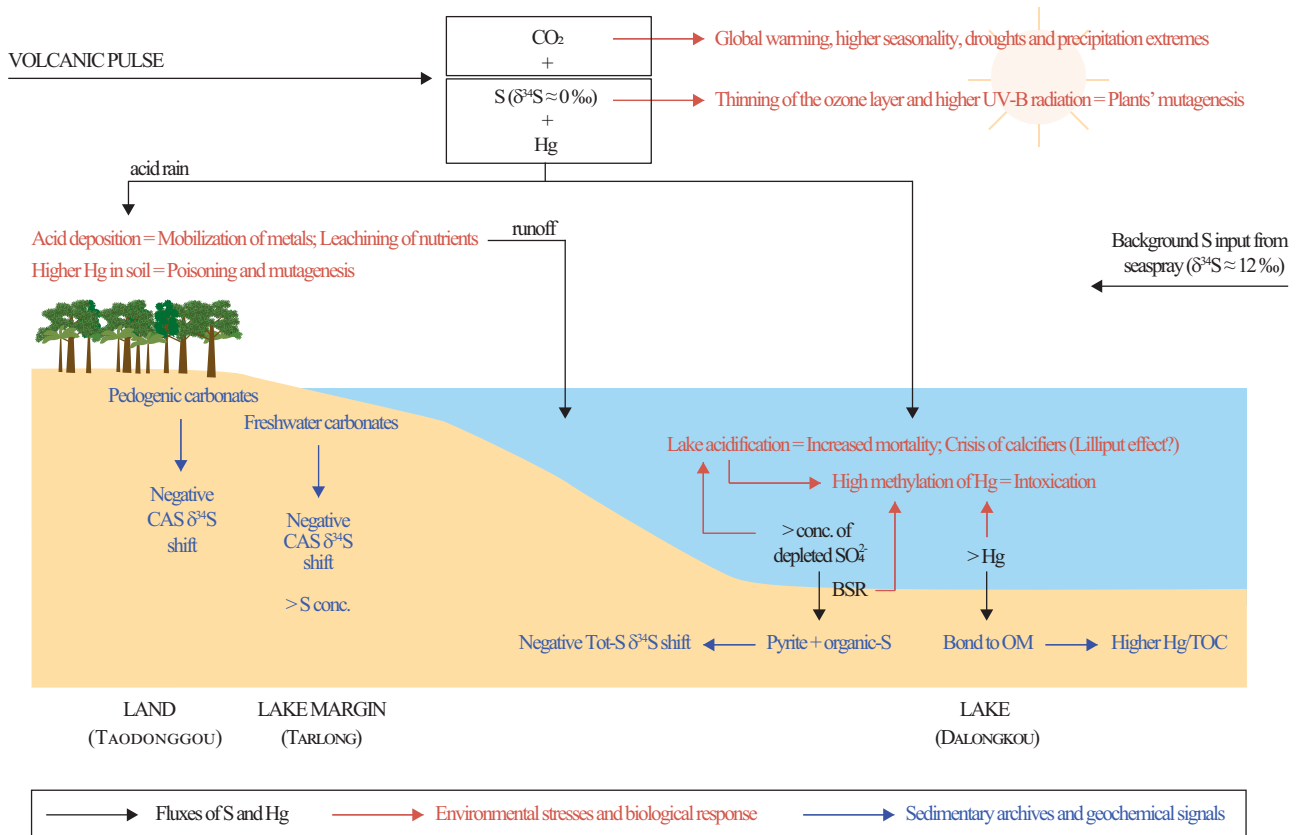


Fig. 6 | Extinction mechanism in the lacustrine ecosystem of the Junggar Basin. Increased volcanic S and Hg in the atmosphere from the Siberian Traps large igneous province caused acid rain, acidification and methylation of Hg that severely

stressed the lacustrine biota. These local effects were coupled with the global effects of volcanic CO_2 input and the consequent environmental changes. Conc. concentration, CAS carbonate-associated sulfate, BSR bacterial sulfate reduction.

before, weathering changes are recorded above the interval with Hg/TOC spikes (and S-isotope shifts) by a switch to coarser sedimentation at the transition from the Guodikeng to the Jiuciyuan Formation, and cannot be the driver of higher Hg loading to the lake.

Paired $\delta^{34}\text{S}_{\text{TOT}}$ and Hg/TOC changes (V1–V6) are recorded in the lower Guodikeng Formation and are coeval with the crisis of the lacustrine ecosystem (Fig. 2)^{28,52,58,59}. The available chemo-, magneto- and bio-stratigraphic constraints^{28,52,60}, and radiometric ages⁶¹ (see “Geological setting” section below for a summary) suggest that the volcanic-driven environmental perturbation in the Junggar Basin started before the 1st NCIE, possibly >300 kyr before the marine extinction at the 2nd NCIE (Fig. 2), similar to the record in the Southern Hemisphere from the Sydney Basin (Fig. 1)³, but before the onset of the terrestrial crisis recorded in South China (ca. 60 kyr before the marine extinction)⁴. Notably, the age of the last coal bed in the Bogda Mountains (northern high latitude) is estimated at 252.29 Ma⁵⁹, which is the same age (252.3 ± 0.3 Ma) of the last coal found in the Sydney basin (southern high latitude)³.

Radioisotope data indicate that the end-Permian terrestrial crisis was linked to the initial, significantly pyroclastic phase of Siberian Traps volcanism⁶², which injected a huge amount of volcanic CO_2 and SO_2 into the atmosphere, as well as metals². Additional S could have been released by the interaction of the ascending magmas with the evaporitic rocks that are abundant in the basin where the Siberian Traps were emplaced²⁴. Evidence of Late Permian strong pulses of silicic arc magmatism has been found around the world at the time of the PTME (Fig. 1; e.g., ref. 63), but the amount of S released from this type of volcanism was likely much lower than that from the Siberian Traps⁶⁴.

Mass balance calculations using the CAS isotope data (see Source Data file) suggest that the volcanic S contribution (range $\delta^{34}\text{S}$ –7.5 to +5‰⁶⁵), increased from 0–25% in the pre-extinction interval to 33–100% during the decrease in $\delta^{34}\text{S}_{\text{CAS}}$ across the terrestrial extinction. These calculations are based on the pre-extinction baseline $\delta^{34}\text{S}_{\text{CAS}}$ of +11 to +12‰ recorded at the base of Taodonggou and Tarlong, and the range of $\delta^{34}\text{S}_{\text{CAS}}$ values between NCIE 1 and 2 during the extinction of +5 to +7.5‰. The nature of the CAS records (see earlier “Discussion”) suggests that they likely record the average background-S loading in the catchment, meaning that the contribution of volcanic-S during individual events could have been greater.

Our Hg record fits well with the timeframe of Siberian Traps emplacement and the global Hg records², supporting previous modeling results¹⁰: Higher loading of volcanic Hg during the terrestrial crisis and the mainly pyroclastic activity of the Siberian Traps would have increased the amount of Hg in the terrestrial reservoir which was then released at the time of the vegetation collapse.

The scenario inferred from our dataset is similar to that proposed for the Karoo Basin, where an increase in S concentrations and negative $\delta^{34}\text{S}$ values in fluvial sediments across the Permo–Triassic boundary were ascribed to high atmospheric deposition due to acid rain²⁴. A record from the Sydney Basin shows a broad negative shift in pyrite $\delta^{34}\text{S}$ starting from near the base of the terrestrial extinction interval, just before the Permian–Triassic boundary, and ending in the Dienerian, with one datapoint showing a very negative value down to –21‰ in the terrestrial crisis interval itself²³. Peaks in Ni/Al and Hg/TOC, which are thought to indicate increased volcanic activity, are found at the end of the terrestrial crisis interval in the same basin^{23,66}. Our high-resolution combined multi-archive S-isotope and bulk Hg records from the Junggar Basin strongly support a link between increases in the input of volcanic gases to the atmosphere and the terrestrial crisis.

Terrestrial minor-S isotope record

The high abundance of teratological sporomorphs in several successions across the PTME has been attributed to increased UV-B radiation due to

the disruption of the ozone layer by stratospheric volcanic emissions of SO_2 and halogens^{13,20,21}. However, teratological sporomorphs alone are not necessarily direct evidence of UV-B radiation, as they could also be the result of the toxic effects of metals on plants^{25,67}. More recently, Liu et al.²² used the concentration of UV-B absorbing compounds in pollen to detect an increase in UV-B during the Permo–Triassic extinction interval. The minor isotopes of sulfur provide one of the few ways to derive direct information about the atmospheric impact of past volcanic activity^{68,69}. The development of a sulfur mass-independent fractionation (S-MIF) signal during the photooxidation of SO_2 is sensitive to its exposure to UV-B radiation⁷⁰: Volcanic SO_2 oxidized below the UV-B absorbing ozone layer does not display S-MIF, but larger eruptions such as Pinatubo, which injected SO_2 into or above the ozone layer show S-MIF signals⁶⁹. S-MIF in isotopes of surface sulfate has been recorded chiefly in Archean rocks⁷¹ but has also been detected as a result of brief SO_2 injection into the upper atmosphere during the Chicxulub impact at the end-Cretaceous event⁷². Terrestrial sediments are thought to be better archives of S-MIF than marine sediments because a number of S-cycle biogeochemical processes can modify the pristine signal in marine environments⁷³. Deviations in the $\Delta^{33}\text{S}$ and $\Delta^{36}\text{S}$ data from Dalongkou North and Tarlong are within the bounds attributable to biological mass-dependent processes only (Supplementary Fig. S4), so no S-MIF is clearly recorded in lake sulfate (Fig. 5). Complete destruction of the ozone layer would produce a large S-MIF signal and can be therefore excluded. However, thinning of the ozone layer²² is still compatible with our S isotope record because it has a more muted effect on UV-B fluxes, likely making S-MIF development less sensitive to partial ozone depletion⁷⁴. Partial depletion of the ozone layer and the resulting increase in UV-B radiation could still have had a huge impact on vegetation.

Mechanism of terrestrial extinction

The use of soil and lake carbonate CAS data is shown to be a powerful tool to explore terrestrial sulfur cycling and to define the isotopic composition of terrestrial sulfate in the past. By performing high-resolution geochemical analysis across the record of the end-Permian terrestrial crisis and defining the full sulfur isotope system, our record provides detailed evidence for the pulsed nature of S addition to the Junggar Basin catchment and clear evidence of its volcanic origin. Our dataset therefore offers a detailed picture of the cascade of events that could have triggered the biological crisis in the study area (Fig. 6). Acid rain, metal poisoning and ozone depletion are the main kill mechanisms proposed for the end-Permian terrestrial crisis². The record from the Junggar Basin provides evidence of multiple discrete pulses of S and Hg deposition, likely driven by Siberian Trap volcanism. These events would have imposed recurring episodes of stress on the terrestrial ecosystem during an interval of ~300 Kyr prior to the marine extinction (Fig. 2).

For example, modern lake-water column acidification is known to have major effects on lacustrine biota, but the severity of this effect depends on the ability of the environment to buffer acidity⁷⁵. While the Junggar catchment contains small amounts of carbonate, it is dominantly siliciclastic in nature with a relatively low buffering capacity and thus may have been more sensitive to acid deposition. Globally, the response to these acid rain pulses would have been quite heterogeneous, with catchment buffering capacity playing a role in determining extinction severity. Acid deposition mobilizes toxic metals such as Al from within catchments, and, in modern studies, acidified lakes show increased fish mortality and reduced biodiversity, with deleterious ecological effects becoming apparent after only small decreases in pH⁷⁶. Moreover, lake-water acidification would have had effects on the ability of calcifying organisms to precipitate carbonate shells leading to their crisis. We can, for instance, speculate that a higher energy cost to produce calcium carbonate shells at decreasing pH⁷⁷ could have induced ostracods to reduce their size, as observed in the Dalongkou lake system (Lilliput effect²⁷; Fig. 2).

It has been shown that in modern acidified lakes, net methylation of inorganic Hg (i.e., the balance between methylation and demethylation) is higher at the sediment-water interface and in the water column^{78–80}. Microbial sulfate reduction is thought to facilitate Hg methylation in acidic lakes and would be stimulated by increased sulfate deposition^{78,80}. Because methylmercury is lipophilic and can easily bind to proteins⁷⁸, it can accumulate in organisms at all trophic levels^{81–83}. Methylmercury is highly toxic to freshwater animals and plants, and for some organisms, it can be lethal even at low concentrations⁸⁴. Atmospheric deposition of volcanic Hg in soil and direct uptake by plants could have also had harmful effects. Hg intoxication of higher plants can modify DNA and result in mutagenesis, inhibit plant growth, and reduce photosynthesis⁸⁵. In this respect, the occurrence of mutated pollen within the interval with Hg and S-isotope anomalies supports metal poisoning as at least a contributing cause of teratology, possibly coupled with ozone layer thinning²², which did not produce resolvable changes in the minor S-isotope signature (Fig. 5).

The deposition of S and other volcanic volatiles is likely to have been highly heterogeneous over the Earth's surface⁸⁶. Emissions of chemical species with shorter atmospheric lifetimes (e.g., SO₂, HCl) from the Siberian Traps could have been particularly concentrated in the Northern Hemisphere¹⁷, where our record (Junggar Basin) was located (Fig. 1). If we assume that the evidence for pulses of Hg and S deposition were also accompanied by pulsed CO₂ emissions the chemical stressors on individual catchments may also be linked to global effects on climate, creating instability expressed as extremes of temperature, precipitation, seasonality and climate variability over short timescales. Repeated pulses of likely volcanic S deposition, as shown from our record, corroborate modeling predictions of “climate swings” (in temperature, hydrological cycle, ocean circulation) caused by outgassing of S and C from the Siberian Traps¹⁷. Concurrently, a partial depletion of the ozone layer, which is not excluded by our minor S-isotope records, could increase UV-B radiation with major consequences for vegetation. Recurrent stress on land during the end of the Permian over a relatively long interval (ca. 60–300 Kyr)—as observed in many different records^{3–7,9,23,87}—driven by the combined global (climate extremes, higher UV-B radiation) and local (e.g., lake acidification and poisoning) effects of repeated injections of volcanic gases from the Siberian Traps into atmosphere, likely prevented the terrestrial ecosystems from adapting to these high-frequency changes, and eventually led to their collapse.

Methods

Sampling and geological setting

We analyzed bulk sediment samples from the Dalongkou North lacustrine section, the nearby wholly terrestrial Tarlong South, and lake marginal Taodonggou (also known as Taoshuyuan) sections for palaeosol carbonates and freshwater limestones (Taodonggou only) encompassing the Wutonggou Fm. (latest Permian) and Guodikeng Fm. (Permo–Triassic boundary) of the Junggar Basin^{28,29}. The sections are located in the foothills of the Bogda Mountains, Xinjiang, Northwest China (Fig. 1). The lacustrine succession of Dalongkou has been proposed as a candidate for the global non-marine Accessory Stratotype Section and Point (ASSP) for the Permo–Triassic boundary (PTB), because of its exceptional exposure, continuity and paleontological record^{52,88}. At Dalongkou North, the PTME is identified by the crisis of Permian conchostracans, ostracods, and *Charophyte* algae within the Guodikeng Fm. (Fig. 2). A Lilliput ostracod fauna and an increase in abundance of *Lycophyte* spores, which indicates the shift to herbaceous-dominated survivor flora after the collapse of late Permian forests, were recorded just above the extinction level²⁷ (Fig. 2). The first occurrence of the vertebrate *Lystrosaurus* and of the megaspore *Oty-nisporites eotriassicus*²¹, coupled to conchostracan, ostracod and sporomorph biostratigraphy^{27,89,90}, allows the placement of the

terrestrial PTB in the upper part of the Guodikeng Fm. ID-TIMS U/Pb analysis of bentonite layers in the section from the Tarlong-Taodonggou graben give ages of 253.11 ± 0.05 Ma and 253.63 ± 0.24 Ma for the lower part of the Guodikeng Formation⁶¹, supporting the biostratigraphic placement of the PTB (ca. 251.9 Ma) in the uppermost portion of this formation. In the middle–upper Guodikeng Fm., mutated (teratological) grains of bisaccate gymnosperm pollen (*Klauspollenites schaubergeri* and *Alisporites* sp.) are more abundant (up to 4% of the total sporomorphs) than in background conditions²¹ (Fig. 2). Abnormal bisaccates, instead of having the two normal air sacs used for pollen dispersal, present one, three or more sacs²¹, which hinders their ability to fertilize female gametes¹³. C-isotope ($\delta^{13}\text{C}$) analysis of bulk organic matter from the Dalongkou North and Taodonggou sections shows distinct C-isotope excursions that can be correlated to the marine records^{21,28,29} (Fig. 2). The sampled parts of the Tarlong South and Taodonggou sections represent lake margin and fluvial/deltaic environments respectively^{29,91}. Permian palaeosol carbonates sampled at the Tarlong South and Taodonggou sections formed in saturated to well-drained soils with a seasonal precipitation regime. Around the PTB, soil types and sediment geochemistry indicate a change to more arid conditions. Soil carbonates that are formed by the replacement of gypsum appear around the PTB interval^{29,91}. Thin lacustrine limestones formed in shallow water at the lake margin in various settings⁹¹ were sampled at regular intervals throughout the Tarlong South section. While the types of carbonates vary, they would all have formed in the presence of lake or soil pore water and thus can be expected to sample ambient terrestrial sulfate. To prepare the samples for geochemical analyses, fresh samples from the Dalongkou, Tarlong and Taodonggou sections were powdered using a TEMA laboratory agate disc mill at the School of Earth and Environment (SEE) of the University of Leeds (UK).

Total organic carbon (TOC) and organic carbon isotope analysis

Rock powders were decarbonated with 10% HCl. The acid-washed residue was rinsed with MilliQ water until neutral and dried. The TOC content was then measured using a LECO® SC-144DR Dual Range carbon and sulfur analyser at SEE (Leeds), and calculated using mass loss after acid digestion. For organic carbon isotope analysis, about 2 g of powder for each sample was weighed and reacted with 4 mol/L HCl for 24 h to remove carbonate, then rinsed with ultrapure water repeatedly until neutralized, and finally dried at 35 °C. The $\delta^{13}\text{C}_{\text{org}}$ was then measured using an elemental analyzer (EA) coupled to an isotope ratio mass spectrometer (Thermo Delta V Advantage) and calibrated using U.S. Geological Survey (USGS) standards: USGS40 ($\delta^{13}\text{C} = -26.39\text{‰}$) and UREA ($\delta^{13}\text{C} = -37.32\text{‰}$). The analytical precision of $\delta^{13}\text{C}_{\text{org}}$ was better than ± 0.2‰. Organic carbon isotope values are given in per mil (‰) relative to Vienna Peedee belemnite (VPDB). All carbon isotope analyses were performed at the State Key Laboratory of Biogeology and Environmental Geology of the China University of Geosciences (Wuhan, China).

Hg concentrations

Hg concentrations were measured with a Lumex RA-915 Portable Mercury Analyzer with PYRO-915 Pyrolyzer at the University of Oxford (UK). For this, 50–250 mg of powdered sample was weighed into a glass boat, placed into the pyrolyzer, and heated to 700 °C. Volatilized elementary Hg was quantified via atomic absorption spectrometry. The instrument was calibrated before use with paint-contaminated soil standards (NIST 2587; 290 ± 9 ppb Hg). At the start of each run and throughout the measurement sequences (every 10 samples), standards were analyzed, using masses ranging from 10 to 90 mg. The analytical precision measured on the standards was within 6%. In sediments, Hg is generally hosted in organic matter^{92,93}. A prevalent sulfidic host phase is found mainly in euxinic depositional palaeoenvironments with sedimentary total sulfur >1%⁹³, which is not the case for the

samples analyzed here. Hg concentrations at Dalongkou North have therefore been normalized for TOC contents >0.2 following the method of Grasby et al.⁹²

Bulk lake sediment sulfur extractions

Reduced metal bound-S (assumed to be pyrite) was extracted using a standard chromium reduction method⁹⁴ with liberated sulfide trapped by a silver nitrate solution as silver sulfide. Concentrations were extremely low (range = 0–12 ppm S, median = 3.4 ppm S; see Source Data file), so total-S was extracted for isotope analysis. This will consist of the sum of metal-bound sulfides, inorganic sulfates and organic-bound sulfur. Total-S was extracted using a modified version of ASTM method D3177⁹⁵. A mixture of ~6 g of sample and 10 g of Eschka's mixture (2 parts MgO and 1 part Na₂CO₃) covered uniformly with an additional ~1 g of Eschka's mixture, was heated in corundum crucibles to 850 °C and held there for 2 h. The resulting solid was extracted using boiling deionized water and then filtered to remove any insoluble residue. After filtration 6–7 mL of 36% HCl was added to each solution and then boiled again before cooling and addition of 20 mL BaCl₂. BaSO₄ was left to precipitate in a refrigerator before separation, followed by cleaning by centrifugation and washing with ultrapure water. The BaSO₄ residue was then dried and weighed for isotope analysis. Blanks were run alongside the samples during total-S extraction, and did not yield any BaSO₄ precipitate.

Carbonate-associated sulfate (CAS) extraction

To extract CAS from palaeosol carbonate nodules and freshwater limestones, we used the method of He et al.⁹⁶. Approximately 10 g of powder was bleached with 6% NaOCl for 48 h in a 50 mL tube to oxidize possible organic sulfur and metastable sulfide minerals to soluble sulfate. The bleached solution was filtered through a 0.2 μm polypropylene membrane syringe filter and then acidified with 6 M HCl. Saturated BaCl₂ was added to the solution, and BaSO₄ was precipitated at -2 °C, over a week. The solid bleached residue was washed in 10% NaCl solution for 24 h five times to remove all soluble sulfate contaminants that were generated during the bleaching process. The washed solid residue was then transferred into a 500 mL tube and treated with 6 M HCl to extract CAS. A larger tube is necessary as the reaction with 6 M HCl can be vigorous. The acid digestion was finished within 20 min to minimize the potential for oxidation of any remaining pyrite. The extracted CAS solution was retained by filtration through 0.2 μm polypropylene membrane syringe filters. Saturated BaCl₂ was then added to the remaining filtered solution and left to precipitate BaSO₄. The resulting BaSO₄ precipitate was repeatedly washed with ultrapure water before being dried, weighed and analyzed for isotopes. The CAS concentrations in all samples were calculated from the amounts of residual BaSO₄ precipitate, and in selected samples, the S concentration was measured with ICP-OES in an aliquot of the filtered solution, which was pipetted before the addition of saturated BaCl₂ and precipitation of BaSO₄. Blanks were not run for the CAS extraction as previous extensive experience of running blanks for this process shows that they do not produce any measurable BaSO₄ as long as the HCl has a specified low S content (<2 mg/L SO₄).

Sulfur isotope measurement

Sulfur isotopic analysis of BaSO₄ precipitate from CAS solution and the bleached filtrate and total S Eschka's solution was carried out in the Cohen lab of SEE (Leeds) using an Elementar Pyrocube coupled to an Isoprime continuous flow mass spectrometer. BaSO₄ precipitates were weighed into an 8 × 5 mm tin cup and combusted at 1150 °C in a flow of helium (CP grade) and pure oxygen (N5.0). Samples were weighed for mass spectrometry in duplicate, aiming for weights in a limited range to produce peak heights of between 2.5 and 3.5 nA. The source is tuned for maximum linearity and repeats of a check standard BaSO₄ with peak heights in the range 2–4 nA had a precision of ±0.3‰ (1 s.d.).

Complete combustion was achieved by passing the gas through tungstic oxide. Excess oxygen was removed from the gas flow using pure copper wires at a temperature of 850 °C, and the water was removed using Sicapent©. The produced SO₂ gas was separated from contaminating N₂ or CO₂ by temperature-controlled adsorption/desorption columns. The δ³⁴S value of the analyzed samples is calculated using the integrated mass 64 and 66 signals relative to those in a SO₂ reference gas (N3.0). These values were calibrated to the international V-CDT scale using a seawater-derived internal BaSO₄ standard, SWS-3 (20.3‰), which has been analyzed against the international standards NBS-127 (20.3‰), NBS-123 (17.01‰), IAEA S-1 (-0.30‰) and IAEA S-3 (-32.06‰), and an inter-lab chalcopyrite standard CP-1 (-4.56‰). The precision obtained for repeat analysis of the internal BaSO₄ standard was ± 0.3‰ (1 sd) or better.

Multiple S-isotope analysis

Quadruple sulfur isotopes were measured at the University of St Andrews using a Curie-point pyrolysis method modified from Ueno et al.⁹⁷, as described in Warke et al.⁹⁸. Briefly, BaSO₄ precipitates were converted to Ag₂S by reduction with a thode solution under a stream of oxygen-free N₂^{99,100}. From 0.3 to 0.5 mg of Ag₂S were weighed into an iron nickel-cobalt alloy pyrofoil with excess CoF₃, and placed in a borosilicate glass tube with ~1 g of optical NaF crystals. The reaction tube was placed in a Curie-point pyrolyzer (JHP-22, Japan Analytical Industry), evacuated down to 10⁻³ mbar, and flash heated at 590 °C for 297 s to produce SF₆ gas. The product gas was introduced into a bespoke vacuum line and purified cryogenically, and by passing through an SRI 8610 C gas chromatograph equipped with a 12 ft HayeSep Q packed column (1/800 OD, 80–100 mesh) and a 12 ft Molecular Sieves 5A° packed column (1/800 OD, 60–80 mesh) operating at a He flow rate of 24 mL/min and a temperature of 80 °C. The resulting purified SF₆ gas was monitored by a thermal conductivity detector (TCD), captured at liquid N₂ temperature into the micro-volume inlet system of a Thermo MAT 253 mass spectrometer and then expanded into the source of the mass spectrometer at room temperature. Sulfur isotope abundances were analyzed on m/z 127, 128, 129 and 131 (corresponding to ³²SF₆⁺, ³³SF₆⁺, ³⁴SF₆⁺, and ³⁶SF₆⁺) and compared to reference SF₆ gas calibrated to V-CDT⁹⁸.

Measured sulfur isotope ratios are reported in the delta notation (δ³³S, δ³⁴S, δ³⁶S) relative to VCDT. For mass-dependent processes δ³³S ≈ 0.515 × δ³⁴S, and δ³⁶S ≈ 1.90 × δ³⁴S³¹. Deviations from these predicted relationships are expressed using Δ³³S and Δ³⁶S notation, where:

$$\Delta^{33}\text{S} = 1000 * \left[\ln \left(\frac{\delta^{33}\text{S}}{1000} + 1 \right) - 0.515 * \ln \left(\frac{\delta^{34}\text{S}}{1000} + 1 \right) \right] \quad (1)$$

$$\Delta^{36}\text{S} = 1000 * \left[\ln \left(\frac{\delta^{36}\text{S}}{1000} + 1 \right) - 1.9 * \ln \left(\frac{\delta^{34}\text{S}}{1000} + 1 \right) \right] \quad (2)$$

The Δ³³S and Δ³⁶S values for IAEA-S1 produced by this method (*n* = 78) are 0.115 ± 0.015‰ and -0.581 ± 0.172‰ (mean ± 1σ). These values overlap, within uncertainty, with values published in the literature^{97,101,102}. The precision of a single measurement (1σ) was typically in the range of 0.01‰ for Δ³³S and 0.1‰ for Δ³⁶S. We do not quote δ³⁴S values from the SF₆ measurements because there is a documented small but variable mass-dependent offset that occurs during the fluorination process. This effect scales with mass and therefore has no effect on the Δ values⁹⁷. Our δ³⁴S data are therefore only derived from the continuous flow SO₂ measurements described in the previous section.

Data availability

All new data presented in this paper are available in the supplementary excel file. Source data are provided with this paper.

References

1. Erwin, D. H. *The Great Paleozoic Crisis: Life and Death in the Permian* (Columbia Univ. Press, 1993).
2. Dal Corso, J. et al. Environmental crises at the Permian–Triassic mass extinction. *Nat. Rev. Earth Environ.* **3**, 197–214 (2022).
3. Fielding, C. R. et al. Age and pattern of the southern high-latitude continental end-Permian extinction constrained by multiproxy analysis. *Nat. Commun.* **10**, 385 (2019).
4. Chu, D. et al. Ecological disturbance in tropical peatlands prior to marine Permian–Triassic mass extinction. *Geology* **48**, 288–292 (2020).
5. Gastaldo, R. A. et al. The base of the Lystrosaurus Assemblage Zone, Karoo Basin, predates the end-Permian marine extinction. *Nat. Commun.* **11**, 1428 (2020).
6. Biswas, R. K., Kaiho, K., Saito, R., Tian, L. & Shi, Z. Terrestrial ecosystem collapse and soil erosion before the end-Permian marine extinction: organic geochemical evidence from marine and non-marine records. *Glob. Planet. Change* **195**, 103327 (2020).
7. Kaiho, K., Aftabuzzaman, M., Jones, D. S. & Tian, L. Pulsed volcanic combustion events coincident with the end-Permian terrestrial disturbance and the following global crisis. *Geology* **49**, 289–293 (2021).
8. Feng, Z. et al. From rainforest to herbland: new insights into land plant responses to the end-Permian mass extinction. *Earth Sci. Rev.* **204**, 103153 (2020).
9. Vajda, V. et al. End-Permian (252 Mya) deforestation, wildfires and flooding—an ancient biotic crisis with lessons for the present. *Earth Planet. Sci. Lett.* **529**, 115875 (2020).
10. Dal Corso, J. et al. Permo–Triassic boundary carbon and mercury cycling linked to terrestrial ecosystem collapse. *Nat. Commun.* **11**, 2962 (2020).
11. Labandeira, C. C. & Sepkoski, J. J. Insect diversity in the fossil record. *Science* **261**, 310–315 (1993).
12. Angielczyk, K. D., Roopnarine, P. D. & Wang, S. C. Modeling the role of primary productivity disruption in end-Permian extinctions. *N. Mex. Mus. Nat. Hist. Sci. Bull.* **30**, 16–23 (2005).
13. Benca, J. P., Duijnste, I. A. P. & Looy, C. V. UV-B-induced forest sterility: implications of ozone shield failure in Earth's largest extinction. *Sci. Adv.* **4**, e1700618 (2018).
14. Zhao, X. et al. Recovery of lacustrine ecosystems after the end-Permian mass extinction. *Geology* **48**, 609–613 (2020).
15. Zheng, D. et al. Middle-Late Triassic insect radiation revealed by diverse fossils and isotopic ages from China. *Sci. Adv.* **4**, eaat1380 (2018).
16. Retallack, G. J., Veevers, J. J. & Morante, R. Global coal gap between Permian–Triassic extinction and Middle Triassic recovery of peat-forming plants. *Geol. Soc. Am. Bull.* **108**, 195–207 (1996).
17. Black, B. A. et al. Systemic swings in end-Permian climate from Siberian Traps carbon and sulfur outgassing. *Nat. Geosci.* **11**, 949–954 (2018).
18. Viglietti, P. A. et al. Evidence from South Africa for a protracted end-Permian extinction on land. *Proc. Natl Acad. Sci. USA* **118**, e2017045118 (2021).
19. Liu, J., Abdala, F., Angielczyk, K. D. & Sidor, C. A. Tetrapod turnover during the Permo–Triassic transition explained by temperature change. *Earth Sci. Rev.* **224**, 103886 (2022).
20. Visscher, H. et al. Environmental mutagenesis during the end-Permian ecological crisis. *Proc. Natl Acad. Sci. USA* **101**, 12952–12956 (2004).
21. Foster, C. B. & Afonin, S. A. Abnormal pollen grains: an outcome of deteriorating atmospheric conditions around the Permian–Triassic boundary. *J. Geol. Soc.* **162**, 653–659 (2005).
22. Liu, F. et al. Dying in the Sun: direct evidence for elevated UV-B radiation at the end-Permian mass extinction. *Sci. Adv.* **9**, eabo6102 (2023).
23. Li, M. et al. Sulfur isotopes link atmospheric sulfate aerosols from the Siberian Traps outgassing to the end-Permian extinction on land. *Earth Planet. Sci. Lett.* **592**, 117634 (2022).
24. Maruoka, T., Koeberl, C., Hancox, P. J. & Reimold, W. U. Sulfur geochemistry across a terrestrial Permian–Triassic boundary section in the Karoo Basin, South Africa. *Earth Planet. Sci. Lett.* **206**, 101–117 (2003).
25. Chu, D. et al. Metal-induced stress in survivor plants following the end-Permian collapse of land ecosystems. *Geology* **49**, 657–661 (2021).
26. Jin, Y. & Shang, Q. The Permian of China and its interregional correlation. *Dev. Palaeontol. Stratigr.* **18**, 71–98 (2000).
27. Chu, D. et al. Lilliput effect in freshwater ostracods during the Permian–Triassic extinction. *Palaeogeogr. Palaeoclimatol. Palaeoecol.* **435**, 38–52 (2015).
28. Cao, C., Wang, W., Liu, L., Shen, S. & Summons, R. E. Two episodes of ^{13}C -depletion in organic carbon in the latest Permian: evidence from the terrestrial sequences in northern Xinjiang, China. *Earth Planet. Sci. Lett.* **270**, 251–257 (2008).
29. Thomas, S. G. et al. Palaeosol stratigraphy across the Permian–Triassic boundary, Bogda Mountains, NW China: implications for palaeoenvironmental transition through earth's largest mass extinction. *Palaeogeogr. Palaeoclimatol. Palaeoecol.* **308**, 41–64 (2011).
30. Wu, Y. et al. Organic carbon isotopes in terrestrial Permian–Triassic boundary sections of North China: implications for global carbon cycle perturbations. *Geol. Soc. Am. Bull.* **132**, 1106–1118 (2020).
31. Ono, S. Photochemistry of sulfur dioxide and the origin of mass-independent isotope fractionation in Earth's atmosphere. *Annu. Rev. Earth Planet. Sci.* **45**, 301–329 (2017).
32. Barkan, Y., Paris, G., Webb, S. M., Adkins, J. F. & Halevy, I. Sulfur isotope fractionation between aqueous and carbonate-associated sulfate in abiotic calcite and aragonite. *Geochim. Cosmochim. Acta* **280**, 317–339 (2020).
33. Howell, K. J. & Bao, H. Caliche as a geological repository for atmospheric sulfate. *Geophys. Res. Lett.* **33**, L13816 (2006).
34. Whelpdale, D. M. An overview of the atmospheric sulphur cycle. *Sulphur Cycling on the Continents* (Wiley, 1992).
35. Bernasconi, S. M. et al. An evaporite-based high-resolution sulfur isotope record of Late Permian and Triassic seawater sulfate. *Geochim. Cosmochim. Acta* **204**, 331–349 (2017).
36. Newman, L., Krouse, H. R. & Grinenko, V. A. Sulphur isotope variations in the atmosphere in *Stable Isotopes in the Assessment of Natural and Anthropogenic Sulphur in the Environment* (Wiley, 1991).
37. Newton, R. & Bottrell, S. Stable isotopes of carbon and sulphur as indicators of environmental change: past and present. *J. Geol. Soc.* **164**, 691–708 (2007).
38. Rech, J. A., Quade, J. & Hart, W. S. Isotopic evidence for the source of Ca and S in soil gypsum, anhydrite and calcite in the Atacama Desert, Chile. *Geochim. Cosmochim. Acta* **67**, 575–586 (2003).
39. Busenberg, E. & Niel Plummer, L. Kinetic and thermodynamic factors controlling the distribution of SO_3^{2-} and Na^+ in calcites and selected aragonites. *Geochim. Cosmochim. Acta* **49**, 713–725 (1985).
40. Paris, G., Fehrenbacher, J. S., Sessions, A. L., Spero, H. J. & Adkins, J. F. Experimental determination of carbonate-associated sulfate $\delta^{34}\text{S}$ in planktonic foraminifera shells. *Geochem. Geophys. Geosyst.* **15**, 1452–1461 (2014).
41. van Dijk, I., de Nooijer, L. J., Boer, W. & Reichart, G. J. Sulfur in foraminiferal calcite as a potential proxy for seawater carbonate ion concentration. *Earth Planet. Sci. Lett.* **470**, 64–72 (2017).
42. Watanabe, T., Naraoka, H., Nishimura, M. & Kawai, T. Biological and environmental changes in Lake Baikal during the late Quaternary

- inferred from carbon, nitrogen and sulfur isotopes. *Earth Planet. Sci. Lett.* **222**, 285–299 (2004).
43. Trust, B. A. & Fry, B. Stable sulphur isotopes in plants: a review. *Plant Cell Environ.* **15**, 1105–1110 (1992).
44. Novák, M., Bottrell, S. H. & Přečková, E. Sulfur isotope inventories of atmospheric deposition, spruce forest floor and living Sphagnum along a NW-SE transect across Europe. *Biogeochemistry* **53**, 23–50 (2001).
45. Nriagu, J. O. & Soon, Y. K. Distribution and isotopic composition of sulfur in lake sediments of northern Ontario. *Geochim. Cosmochim. Acta* **49**, 823–834 (1985).
46. Mitchell, M. J., Owen, J. S. & Schindler, S. C. Factors affecting sulfur incorporation into lake sediments: paleoecological implications. *J. Paleolimnol.* **4**, 1–22 (1990).
47. Urban, N. R., Ernst, K. & Bernasconi, S. Addition of sulfur to organic matter during early diagenesis of lake sediments. *Geochim. Cosmochim. Acta* **63**, 837–853 (1999).
48. Rudd, J. W. M., Kelly, C. A. & Furutani, A. The role of sulfate reduction in long term accumulation of organic and inorganic sulfur in lake sediments. *Limnol. Oceanogr.* **31**, 1281–1291 (1986).
49. Fry, B. Stable sulfur isotopic distributions and sulfate reduction in lake sediments of the Adirondack Mountains, New York. *Biogeochemistry* **2**, 329–343 (1986).
50. Bottrell, S. H. & Raiswell, R. Sulphur isotopes and microbial sulphur cycling in sediments in *Microbial Sediments* (Springer, 2000).
51. Mayer, B., Alpay, S., Gould, W. D., Lortie, L. & Rosa, F. The onset of anthropogenic activity recorded in lake sediments in the vicinity of the Horne smelter in Quebec, Canada: sulfur isotope evidence. *Appl. Geochem.* **22**, 397–414 (2007).
52. Metcalfe, I. et al. Stratigraphy, biostratigraphy and C-isotopes of the Permian-Triassic non-marine sequence at Dalongkou and Lucaogou, Xinjiang Province, China. *J. Asian Earth Sci.* **36**, 503–520 (2009).
53. Pasquier, V. et al. Pyrite sulfur isotopes reveal glacial-interglacial environmental changes. *Proc. Natl Acad. Sci. USA* **114**, 5941–5945 (2017).
54. Berner, R. A. & Raiswell, R. C/S method for distinguishing freshwater from marine sedimentary rocks. *Geology* **12**, 365–368 (1984).
55. Algeo, T. J., Luo, G. M., Song, H. Y., Lyons, T. W. & Canfield, D. E. Reconstruction of secular variation in seawater sulfate concentrations. *Biogeosciences* **12**, 2131–2151 (2015).
56. Sanei, H., Grasby, S. E. & Beauchamp, B. Latest Permian mercury anomalies. *Geology* **40**, 63–66 (2012).
57. Grasby, S. E. et al. Isotopic signatures of mercury contamination in latest Permian oceans. *Geology* **45**, 55–58 (2017).
58. Shen, J. et al. Mercury evidence of intense volcanic effects on land during the Permian-Triassic transition. *Geology* **47**, 1117–1121 (2019).
59. Yang, W. et al. Paleoenvironmental and paleoclimatic evolution and cyclo- and chrono-stratigraphy of upper Permian-Lower Triassic fluvial-lacustrine deposits in Bogda Mountains, NW China—implications for diachronous plant evolution across the Permian-Triassic boundary. *Earth Sci. Rev.* **222**, 103741 (2021).
60. Glen, J. M. G. et al. Magnetostratigraphic correlations of Permian-Triassic marine-to-terrestrial sections from China. *J. Asian Earth Sci.* **36**, 521–540 (2009).
61. Yang, W. et al. Depositional environments and cyclo- and chrono-stratigraphy of uppermost Carboniferous-Lower Triassic fluvial-lacustrine deposits, southern Bogda Mountains, NW China—a terrestrial palaeoclimatic record of mid-latitude NE Pangea. *Glob. Planet. Change* **73**, 15–113 (2010).
62. Burgess, S. D. & Bowering, S. A. High-precision geochronology confirms voluminous magmatism before, during, and after Earth's most severe extinction. *Sci. Adv.* **1**, e1500470 (2015).
63. Chapman, T., Milan, L. A., Metcalfe, I., Blevin, P. L. & Crowley, J. Pulses in silicic arc magmatism initiate end-Permian climate instability and extinction. *Nat. Geosci.* **15**, 411–416 (2022).
64. Self, S., Schmidt, A. & Mather, T. A. Emplacement characteristics, time scales, and volcanic gas release rates of continental flood basalt eruptions on Earth in *Volcanism, Impacts, and Mass Extinctions: Causes and Effects* (Geological Society of America, 2014).
65. Black, B. A., Lamarque, J. F., Shields, C. A., Elkins-Tanton, L. T. & Kiehl, J. T. Acid rain and ozone depletion from pulsed Siberian Traps magmatism. *Geology* **42**, 67–70 (2014).
66. Shen, J. et al. Mercury evidence from southern Pangea terrestrial sections for end-Permian global volcanic effects. *Nat. Commun.* **14**, 6 (2023).
67. Lindström, S. et al. Volcanic mercury and mutagenesis in land plants during the end-Triassic mass extinction. *Sci. Adv.* **5**, eaaw4018 (2019).
68. Baroni, M., Thiemens, M. H., Delmas, R. J. & Savarino, J. Mass-independent sulfur isotopic compositions in stratospheric volcanic eruptions. *Science* **315**, 84–87 (2007).
69. Savarino, J., Romero, A., Cole-Dai, J., Bekki, S. & Thiemens, M. H. UV induced mass-independent sulfur isotope fractionation in stratospheric volcanic sulfate. *Geophys. Res. Lett.* **30**, 2131 (2003).
70. Claire, M. W. et al. Modeling the signature of sulfur mass-independent fractionation produced in the Archean atmosphere. *Geochim. Cosmochim. Acta* **141**, 365–380 (2014).
71. Farquhar, J., Bao, H. & Thiemens, M. Atmospheric influence of Earth's earliest sulfur cycle. *Science* **289**, 756–758 (2000).
72. Junium, C. K. et al. Massive perturbations to atmospheric sulfur in the aftermath of the Chicxulub impact. *Proc. Natl Acad. Sci. USA* **119**, e2119194119 (2022).
73. Halevy, I. Production, preservation, and biological processing of mass-independent sulfur isotope fractionation in the Archean surface environment. *Proc. Natl Acad. Sci. USA* **110**, 17644–17649 (2013).
74. Pavlov, A. A. & Kasting, J. F. Mass-independent fractionation of sulfur isotopes in Archean sediments: strong evidence for an anoxic Archean atmosphere. *Astrobiology* **2**, 27–41 (2002).
75. Clair, T. A., Dennis, I. F., Scruton, D. A. & Gilliss, M. Freshwater acidification research in Atlantic Canada: a review of results and predictions for the future. *Environ. Rev.* **15**, 153–167 (2007).
76. Schindler, D. W. et al. Long-term ecosystem stress: the effects of years of experimental acidification on a small lake. *Science* **228**, 1395–1401 (1985).
77. Spalding, C., Finnegan, S. & Fischer, W. W. Energetic costs of calcification under ocean acidification. *Glob. Biogeochem. Cycles* **31**, 866–877 (2017).
78. Ullrich, S. M., Tanton, T. W. & Abdrashitova, S. A. Mercury in the aquatic environment: a review of factors affecting methylation. *Crit. Rev. Environ. Sci. Technol.* **31**, 241–293 (2001).
79. Gilmour, C. C. & Henry, E. A. Mercury methylation in aquatic systems affected by acid deposition. *Environ. Pollut.* **71**, 131–169 (1991).
80. Gilmour, C. C., Henry, E. A. & Ralph, M. Sulfate stimulation of mercury methylation in freshwater sediments. *Environ. Sci. Technol.* **26**, 2281–2287 (1992).
81. Little, M. E., Burgess, N. M., Broders, H. G. & Campbell, L. M. Mercury in little brown bat (*Myotis lucifugus*) maternity colonies and its correlation with freshwater acidity in Nova Scotia, Canada. *Environ. Sci. Technol.* **49**, 2059–2065 (2015).
82. Wyn, B., Kidd, K. A., Burgess, N. M. & Allen Curry, R. Mercury biomagnification in the food webs of acidic lakes in Kejimikujik National Park and National Historic Site, Nova Scotia. *Can. J. Fish. Aquat. Sci.* **66**, 1532–1545 (2009).

83. Brown, D., Goncharov, A., Paul, E., Simonin, H. & Carpenter, D. O. The relationship between Adirondack lake pH and levels of mercury in yellow perch. *J. Aquat. Anim. Health* **22**, 280–290 (2010).
84. Boening, D. W. Ecological effects, transport, and fate of mercury: a general review. *Chemosphere* **40**, 1335–1351 (2000).
85. Azevedo, R. et al. Inorganic Hg toxicity in plants: a comparison of different genotoxic parameters. *Plant Physiol. Biochem.* **125**, 247–254 (2018).
86. Schmidt, A. et al. Selective environmental stress from sulphur emitted by continental flood basalt eruptions. *Nat. Geosci.* **9**, 77–82 (2016).
87. Mays, C. et al. Refined Permian-Triassic floristic timeline reveals early collapse and delayed recovery of south polar terrestrial ecosystems. *Geol. Soc. Am. Bull.* **132**, 1489–1513 (2020).
88. Cheng, Z. & Lucas, S. G. A possible nonmarine GSSP for the Permian-Triassic boundary. *Albertiana* **12**, 39–44 (1993).
89. Hou, J. P. Two spore-pollen assemblages of Guodikeng formation and discussion on the Permo-Triassic boundary in Junggar Basin, Xinjiang. *Prof. Pap. Stratigr. Palaeontol.* **28**, 177–204 (2004).
90. Kozur, H. W. & Weems, R. E. Detailed correlation and age of continental late Changhsingian and earliest Triassic beds: implications for the role of the Siberian Trap in the Permian-Triassic biotic crisis. *Palaeogeogr. Palaeoclimatol. Palaeoecol.* **308**, 22–40 (2011).
91. Yang, W. et al. Sedimentary evidence of Early-Late Permian mid-latitude continental climate variability, southern Bogda Mountains, NW China. *Palaeogeogr. Palaeoclimatol. Palaeoecol.* **252**, 239–258 (2007).
92. Grasby, S. E., Them, T. R., Chen, Z., Yin, R. & Ardakani, O. H. Mercury as a proxy for volcanic emissions in the geologic record. *Earth Sci. Rev.* **196**, 102880 (2019).
93. Shen, J. et al. Sedimentary host phases of mercury (Hg) and implications for use of Hg as a volcanic proxy. *Earth Planet. Sci. Lett.* **543**, 116333 (2020).
94. Canfield, D. E., Raiswell, R., Westrich, J. T., Reaves, C. M. & Berner, R. A. The use of chromium reduction in the analysis of reduced inorganic sulfur in sediments and shales. *Chem. Geol.* **54**, 149–155 (1986).
95. *Subcommittee D05.21, Annual Book of ASTM Standards, Part 26: Gaseous Fuels; Coal and Coke; Atmospheric Analysis.* (American Society for Testing and Materials, 1977).
96. He, T. et al. An enormous sulfur isotope excursion indicates marine anoxia during the end-Triassic mass extinction. *Sci. Adv.* **6**, eabb6704 (2020).
97. Ueno, Y., Aoyama, S., Endo, Y., Matsu'ura, F. & Foriel, J. Rapid quadruple sulfur isotope analysis at the sub-micromole level by a flash heating with CoF₃. *Chem. Geol.* **419**, 29–35 (2015).
98. Warke, M. R. et al. The great oxidation event preceded a paleoproterozoic 'snowball earth'. *Proc. Natl Acad. Sci. USA* **117**, 13314–13320 (2020).
99. Thode, H. G., Monster, J. & Dunford, H. B. Sulphur isotope geochemistry. *Geochim. Cosmochim. Acta* **25**, 159–174 (1961).
100. Arnold, G. L., Brunner, B., Müller, I. A. & Røy, H. Modern applications for a total sulfur reduction distillation method—what's old is new again. *Geochem. Trans.* **15**, 4 (2014).
101. Ono, S., Wing, B., Rumble, D. & Farquhar, J. High precision analysis of all four stable isotopes of sulfur (³²S, ³³S, ³⁴S and ³⁶S) at nanomole levels using a laser fluorination isotope-ratio-monitoring gas chromatography-mass spectrometry. *Chem. Geol.* **225**, 30–39 (2006).
102. Defouilloy, C., Cartigny, P., Assayag, N., Moynier, F. & Barrat, J. A. High-precision sulfur isotope composition of enstatite meteorites and implications of the formation and evolution of their parent bodies. *Geochim. Cosmochim. Acta* **172**, 393–409 (2016).
103. Boucot, A. J., Xu, C. & Scotese, C. R. *Phanerozoic Paleoclimate: An Atlas of Lithologic Indicators of Climate*, Vol. 11 (SEPM Society for Sedimentary Geology, 2013).
104. Cai, Y. F. et al. Wildfires and deforestation during the Permian-Triassic transition in the southern Junggar Basin, Northwest China. *Earth Sci. Rev.* **218**, 103670 (2021).

Acknowledgements

This work has been funded by the “Ecosystem resilience and recovery from the Permo-Triassic crisis” project (EcoPT; NERC grant number NE/P013724/1, P.I. = P.B.W.), which was a part of the NERC and NSFC-funded Biosphere Evolution, Transitions and Resilience (BETR) programme, and by NSFC 42030513 (P.I. = J.T.).

Author contributions

P.B.W., R.J.N. and J.T. provided the funding. R.J.N., P.B.W. and J.D.C. planned the study. D.C., Y.W., W.S., R.J.N., T.G. and I.M. collected the samples. J.D.C. processed the samples for the analyses with help from T.H. for CAS extraction, and H.A.C. and M.N. for total S extraction. J.D.C. measured TOC. J.D.C. and T.A.M. measured Hg. R.A.J., R.J.N. and J.D.C. measured total and CAS δ³⁴S. J.D.C., T.D.R., M.W.C. and A.L.Z. measured minor S-isotopes. J.D.C. and R.J.N. wrote the manuscript. A.L.Z., D.C., H.-J.S., H.-Y.S., L.T., J.T., T.D.R., M.W.C., T.A.M., T.H., T.G., W.S., Y.W., S.H.B., I.M., H.A.C., M.N., R.A.J. and P.B.W. revised the manuscript.

Competing interests

The authors declare no competing interests.

Additional information

Supplementary information The online version contains supplementary material available at <https://doi.org/10.1038/s41467-024-51671-5>.

Correspondence and requests for materials should be addressed to Jacopo Dal Corso or Robert J. Newton.

Peer review information *Nature Communications* thanks Christopher Fielding, Guillaume Paris and the other anonymous reviewers for their contribution to the peer review of this work. A peer review file is available.

Reprints and permissions information is available at <http://www.nature.com/reprints>

Publisher's note Springer Nature remains neutral with regard to jurisdictional claims in published maps and institutional affiliations.

Open Access This article is licensed under a Creative Commons Attribution-NonCommercial-NoDerivatives 4.0 International License, which permits any non-commercial use, sharing, distribution and reproduction in any medium or format, as long as you give appropriate credit to the original author(s) and the source, provide a link to the Creative Commons licence, and indicate if you modified the licensed material. You do not have permission under this licence to share adapted material derived from this article or parts of it. The images or other third party material in this article are included in the article's Creative Commons licence, unless indicated otherwise in a credit line to the material. If material is not included in the article's Creative Commons licence and your intended use is not permitted by statutory regulation or exceeds the permitted use, you will need to obtain permission directly from the copyright holder. To view a copy of this licence, visit <http://creativecommons.org/licenses/by-nc-nd/4.0/>.

© The Author(s) 2024